



ORIGINAL ARTICLE

J. D. Evans · I. L. Palhares Junior · C. M. Oishi · F. Ruano Neto

Analysis of Newtonian fluid flows around sharp corners with slip boundary conditions

Received: 24 April 2025 / Accepted: 4 September 2025

© The Author(s), under exclusive licence to Springer-Verlag GmbH Germany, part of Springer Nature 2025

Abstract This study examines the asymptotic and numerical behaviour of Newtonian fluid flows in geometries with sharp corners and the influence of the Navier slip boundary condition. A new similarity solution for a reentrant corner flow is derived by introducing a modification to the classical Navier slip law, where the slip coefficient is modelled as a function of the radial distance along the walls from the reentrant corner. This spatially dependent slip coefficient interpolates between the well-known no-slip similarity solution and the constant slip coefficient case in which the walls behave locally as free surfaces. The stress and pressure singularities now depend on the slip coefficient and the similarity solution is validated numerically through flow simulations in an L-shaped domain. This modified slip coefficient is then used to numerically investigate the influence of the corner stress singularity on the global flow behaviours of two benchmark problems: the 4:1 planar contraction flow and the 1:4 planar expansion flow. Specifically, its effect on salient vortex size and intensity, Couette correction and the flow type (extensional, shear or rotation). This combined asymptotic and numerical framework provides new insights into the role of boundary conditions in controlling flow behaviour near singular geometries, which has not previously been investigated.

Keywords Slip flow · Singularity · Reentrant corner flow · Asymptotics

1 Introduction

The mathematical analysis of applying boundary conditions on solid surfaces in fluid flows presents significant complexity, combining challenges from classical continuum mechanics with molecular effects arising at the microscopic scale. A common initial approach when studying the Navier-Stokes equations involves assuming the no-slip boundary condition, meaning that the relative velocity between the solid surface and the fluid is zero in the tangential direction of the flow. This assumption has been widely debated from both theoretical and experimental perspectives, even within the context of Newtonian fluids, leading to the need for further

J. D. Evans
Department of Mathematical Sciences, University of Bath, Bath BA2 7AY, United Kingdom
E-mail: masjde@bath.ac.uk

I. L. Palhares Junior (✉) · C. M. Oishi
Departamento de Matemática e Computação, Faculdade de Ciências e Tecnologia, Universidade Estadual Paulista ‘Júlio de Mesquita Filho’, 19060-900 Presidente Prudente, São Paulo, Brazil
E-mail: irineu.palhares@unesp.br

C. M. Oishi
E-mail: cassio.oishi@unesp.br

F. Ruano Neto
Instituto de Ciências Matemáticas e Computação, Universidade de São Paulo, 13566-590 São Carlos, Brazil
E-mail: fabianoruano@gmail.com

investigation into the so-called “wall slip condition”. In cases such as microfluidics of Newtonian fluids, for instance, experiments have suggested the breakdown of the no-slip condition, i.e., fluid velocity at the wall is non-zero, which may also occur in gas flow and polymer solutions [23]. However, Navier [27] proposed that a fluid does not necessarily adhere completely to a solid boundary but can exhibit a nonzero tangential velocity, which is proportional to the shear rate at the surface [1].

Following earlier reviews on Newtonian fluids (e.g., [28]), recent studies have extended the scope of slip flow analysis to address practical problems of considerable complexity. In [21], a spectral method was employed to investigate viscoelastic flows with slip in porous media, while Drapaca [7] applied the concept of Caputo fractional derivatives combined with slip boundary conditions to numerically model cerebral microaneurysms. Additionally, [19] examined the behaviour of Newtonian, power-law, and Carreau-Yasuda fluids under slip boundary conditions in planar contraction flow, identifying the Carreau-Yasuda model as particularly significant due to observed changes in azimuthal velocity direction, which are associated with boundary slip at high stress levels. Ferrás has also contributed to this field by investigating complex geometries, such as contraction [14] and expansion [15], under slip boundary conditions. These studies provide numerical analyses for both Newtonian and viscoelastic Phan-Thien-Tanner fluids. Convergence for the viscoelastic fluid proved unattainable at high Deborah numbers, particularly when larger slip coefficients were considered. This issue is attributed to steep stress gradients near the reentrant corner singularity.

In addition to numerical studies, some theoretical advancements have been made in understanding flows with slip conditions. Notably, Salamon et al. [32, 33] investigated local similarity solutions for both Newtonian and viscoelastic Oldroyd-B flows within the framework of partial-slip/slip problems, a specific variation of stick-slip flow in which the fluid is allowed to slip along the die wall. Their work provided asymptotic expressions for the streamfunction ψ as a function of the polar coordinate r , demonstrating a behaviour of $\psi \sim \mathcal{O}(r)$ for both Newtonian and viscoelastic flows. Furthermore, they identified a singularity in the non-Newtonian stress tensor $\boldsymbol{\tau}^P$, with $\boldsymbol{\tau}^P \sim \mathcal{O}(\ln(r))$, in the presence of both a Newtonian and the actual velocity field. It is important to emphasize that, in partial-slip/slip flows, the inclusion of a second term in the asymptotic expansion of ψ is required, as the leading term, $\psi \sim \mathcal{O}(r)$, alone does not generate a stress singularity. For flows through reentrant corners, Salamon et al. [34] suggest that, at leading order, corner flows with slip conditions behave similarly to flows over a shear-free surface. Specifically, the eigenvalues (represented by n) of the stream function, $\psi \sim \mathcal{O}(r^n)$, are given by the relation $(n - 1) \cos\left(\frac{\alpha}{2}n\right) \cos\left((n - 2)\frac{\alpha}{2}\right) = 0$, where α is the corner angle. Moreover, the use of slip boundary conditions leads to a more singular local behaviour of velocity gradients and pressure compared to flows governed by no-slip boundary conditions.

Despite these advancements in the asymptotic analysis of slip flows, further investigations remain crucial to refine boundary condition models across various fluid dynamics scenarios. This is essential not only for advancing fundamental understanding but also for addressing practical engineering challenges. However, the phenomenon of wall slip is predominantly observed and studied in non-Newtonian fluids, such as polymer solutions [3, 13, 18, 20, 30]. This explains the scarcity of experimental data for wall slip in Newtonian fluids under the conditions investigated in our paper. Therefore, our study serves as a foundational work by establishing a clear baseline that will enable future experimental and numerical investigations both for Newtonian and, subsequently, non-Newtonian fluids. In this context, the current study follows the works of Dean [6] and Moffat [26] to develop a new slip coefficient-dependent similarity solution for the linear Navier slip law, applied to Newtonian fluids. This is the focus of section 3. However, this study also enhances the understanding of fluid behaviour in domains with corner singularities. This is achieved by quantifying the role of corner singularities on global flow features associated with the two benchmark cases of planar contraction and expansion flows. This is studied in section 4 and is an aspect not previously investigated.

2 Governing equations

The governing equations considered in this study are the mass and momentum conservation equations, expressed as follows:

$$\begin{aligned} \nabla \cdot \mathbf{v} &= 0, \\ \rho \left(\frac{\partial \mathbf{v}}{\partial t} + (\mathbf{v} \cdot \nabla) \mathbf{v} \right) &= -\nabla p + \nabla \cdot \boldsymbol{\tau}, \end{aligned} \quad (1)$$

where \mathbf{v} is the fluid velocity, p is the pressure, ρ is the fluid density, and $\boldsymbol{\tau}$ is the extra-stress tensor. For Newtonian fluids, the extra-stress tensor is given by

$$\boldsymbol{\tau} = 2\mu \mathbf{D}, \quad (2)$$

where μ is the dynamic viscosity and $\mathbf{D} = \frac{1}{2}(\nabla \mathbf{v} + \nabla \mathbf{v}^T)$ is the rate of strain tensor.

We will be concerned with fixed domains with solid walls and now discuss the boundary conditions. On the solid boundaries we denote a unit tangent \mathbf{t} and unit inward normal into the fluid by \mathbf{n} . The walls are non-permeable and solid so that we have the normal flow condition

$$\mathbf{v} \cdot \mathbf{n} = 0. \quad (3)$$

and in addition, we are interested in replacing the usual no-slip condition with a Navier slip condition. We take the latter in the form

$$\mathbf{v} \cdot \mathbf{t} = \kappa (\mathbf{t} \cdot \mathbf{n} : \boldsymbol{\tau}),$$

where κ is the slip coefficient or equivalently

$$\mathbf{v}_{wall} = \kappa \{ \mathbf{n}^T \cdot \boldsymbol{\tau} - [(\mathbf{n}^T \cdot \boldsymbol{\tau}) \cdot \mathbf{n}] \mathbf{n} \}. \quad (4)$$

To express these equations in dimensionless form, the following characteristic scales are introduced:

$$\mathbf{v}^* = \frac{\mathbf{v}}{U}, \quad p^* = \frac{L}{\mu U} p, \quad \mathbf{x}^* = \frac{\mathbf{x}}{L}, \quad t^* = t \frac{U}{L}, \quad \boldsymbol{\tau}^* = \frac{L}{\mu U} \boldsymbol{\tau}, \quad \kappa^* = \frac{\mu}{L} \kappa, \quad (5)$$

where L is the characteristic length scale, and U is the characteristic velocity scale. The pressure scaling is taken consistent with the viscous stress terms, appropriate for Stokes flow. Substituting the relations in Eq. (5) into Eq. (1), and incorporating the stress definition in Eq. (2), the resulting dimensionless equations (dropping the “*” superscripts for simplicity) are:

$$\begin{aligned} \nabla \cdot \mathbf{v} &= 0, \\ Re \left(\frac{\partial \mathbf{v}}{\partial t} + (\mathbf{v} \cdot \nabla) \mathbf{v} \right) &= -\nabla p + \nabla^2 \mathbf{v}, \end{aligned} \quad (6)$$

where $Re = \frac{UL\rho}{\mu}$ is the Reynolds number, representing the ratio of inertial forces to viscous forces in the flow. The wall conditions are given by Eqs. (3) and (4), with all quantities now being dimensionless, i.e., Eq. (3) remains unchanged while the Navier slip boundary condition (4) assumes the form

$$\mathbf{v}_{wall} = 2\kappa \{ \mathbf{n}^T \cdot \mathbf{D} - [(\mathbf{n}^T \cdot \mathbf{D}) \cdot \mathbf{n}] \mathbf{n} \}. \quad (7)$$

3 Stokes flow with Navier slip

3.1 Similarity solutions

We consider first planar Stokes flow around a sharp 270° angled corner relevant to contraction/expansion flow and L-shaped geometries. We present the analytical results generally, taking the corner angle to be α , although the benchmark value of $\alpha = 3\pi/2$ will be of primary focus for the numerical simulations. It is well known that the stream function ψ satisfies the biharmonic equation, which admits separable solutions¹ in polar coordinates of the form [6,26]

$$\psi = C_0 r^{n+1} f(\theta), \quad (8)$$

where C_0 is a constant that is determined by flow away from the corner, with its sign giving the flow direction and n is a constant to be determined. The general form of the function $f(\theta)$ involves four arbitrary constants, A, B, C, D and is given by

$$f(\theta) = A \cos(n+1)\theta + B \sin(n+1)\theta + C \cos(n-1)\theta + D \sin(n-1)\theta. \quad (9)$$

¹ These may also be termed similarity solutions in keeping with, e.g. [26]. The reason being that the PDE problem for the stream function ψ reduces to an ODE for one of the separable functions $f(\theta)$. This reduction in dimensionality of the problem is the common distinguishing feature of similarity (or self-similar) solutions, see e.g. [2]

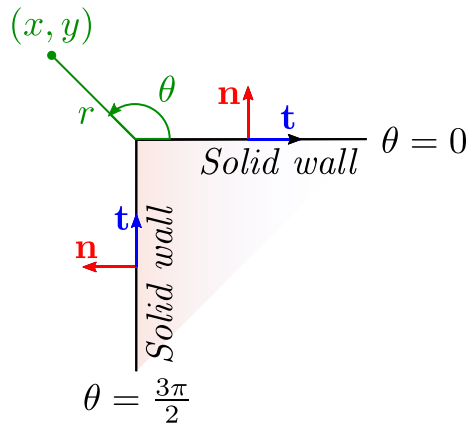


Fig. 1 Coordinate geometry local to the reentrant corner. The corner angle depicted is the 270° benchmark case $\alpha = 3\pi/2$ with $\theta = 0$ the upstream wall and $\theta = \alpha = 3\pi/2$ the downstream wall

Determining n and $f(\theta)$ constitutes an eigenvalue problem, requiring four linearly independent boundary conditions, usually with two furnished on each wall. To fix the geometry, depicted in Figure 1, we designate the upstream wall as $\theta = 0$, the downstream wall at $\theta = \alpha = 3\pi/2$ and take polar coordinates centred at the corner apex. In terms of the polar velocity components, the conditions of impermeability Eq. (3) and slip Eq. (4) on the two boundaries become

$$\text{On } \theta = 0 \text{ or } \alpha \quad v_\theta = 0, \quad v_r = \pm \kappa \frac{1}{r} \frac{\partial v_r}{\partial \theta}, \quad (10)$$

with the positive sign choice on the upstream wall $\theta = 0$ and negative sign on the downstream wall $\theta = \alpha$. These may be written in terms of the streamfunction using

$$v_r = \frac{1}{r} \frac{\partial \psi}{\partial \theta}, \quad v_\theta = -\frac{\partial \psi}{\partial r}, \quad (11)$$

and for the separable solutions Eq. (11) give

$$\text{On } \theta = 0 \text{ or } \alpha \quad f(\theta) = 0, \quad rf'(\theta) = \pm \kappa f''(\theta). \quad (12)$$

We note that the slip condition in Eq. (12) is not separable and thus a true similarity solution does not exist in this form. However, allowing the slip coefficient to depend linearly on the radial distance along the wall, will allow us to generate genuine similarity solutions. Nevertheless, before introducing this modification we discuss the simplified cases already considered in the literature.

3.1.1 The shear-free and no-slip cases

If we consider the asymptotic limit $r \rightarrow 0$ for the slip condition in Eq. (12), then at leading order we obtain the shear-free condition $f'' = 0$. Thus, as noted by Salamon et al. [34], under a constant slip coefficient, the slip surface is behaving as a free-surface close to the corner apex. The solution in this case is given by the flow between two free surfaces, for which the eigenvalues satisfy the transcendental equation

$$\cos(2\alpha) = \cos(2\alpha n),$$

and associated eigenfunction coefficients are

$$\begin{aligned} A &= -C = 0, \\ B &= -2n \sin((n-1)\alpha), \\ D &= 2n \sin((n+1)\alpha). \end{aligned}$$

The eigenvalues in this case are $n = \pm 1 + k\frac{\pi}{\alpha}$, for integer k , the smallest admissible ones as noted by Moffatt being

$$n = \begin{cases} 1 - \pi/\alpha & \text{if } \alpha > \pi \\ -1 + \pi/\alpha & \text{if } \alpha \leq \pi \end{cases}. \quad (13)$$

For the 270° case, $\alpha = 3\pi/2$ and $n = 1/3$.

In contrast to this case, setting the slip coefficient to zero in Eq. (12) gives the no-slip condition $f' = 0$. The eigenvalues in this case satisfy the transcendental equation [6]

$$n^2(1 - \cos(2\alpha)) = 1 - \cos(2n\alpha), \quad (14)$$

and the coefficients of the eigenfunctions are

$$\begin{aligned} A &= -C = \sin(\alpha n) \cos(\alpha) - n \cos(\alpha n) \sin(\alpha), \\ B &= -(n-1) \sin(\alpha) \sin(\alpha n) \\ D &= (n+1) \sin(\alpha) \sin(\alpha n). \end{aligned}$$

The equation (14) can be written as

$$\sin(\alpha n) = \pm \alpha \sin(n),$$

and gives two distinct sets of eigenvalues, one set associated with antisymmetric flow and other symmetric flow, as noted by Moffatt [26]. For our purposes, we are interested in the smallest admissible eigenvalue for $\alpha = 3\pi/2$, which is $n = 0.5444837$ occurring in antisymmetric flow.

3.1.2 A varying slip coefficient similarity solution

To generate genuine separable solutions in the slip case, we propose to study a varying slip coefficient in the form

$$\kappa = \kappa_0 r, \quad (15)$$

where the parameter κ_0 is now the slip constant. The idea of varying spatially the slip behaviour near a stress singularity is proposed in [22] for further regularization of the moving contact line problem. Here, the stress singularity and boundaries are fixed, but such a behaviour will allow us to interpolate smoothly between the no-slip and free-surface behaviours of the previous section.

In this case the boundary conditions in Eq. (4) separate and become

$$\text{On } \theta = 0 \text{ or } \alpha \quad f(\theta) = 0, \quad f'(\theta) = \pm \kappa_0 f''(\theta). \quad (16)$$

The eigenvalues satisfy the transcendental equation

$$4\kappa_0^2 n^2 (\cos(2\alpha) - \cos(2\alpha n)) + 4\kappa_0 n (\sin(2\alpha) - \sin(2\alpha n)) + n^2 (1 - \cos(2\alpha)) = 1 - \cos(2\alpha n) \quad (17)$$

and the coefficients of the eigenfunctions are

$$\begin{aligned} A &= -C = \sin(\alpha n) \cos(\alpha) - n \cos(\alpha n) \sin(\alpha), \\ B &= -(n-1) \sin(\alpha) \sin(\alpha n) - 2n\kappa_0 \sin((n-1)\alpha) \\ D &= (n+1) \sin(\alpha) \sin(\alpha n) + 2n\kappa_0 \sin((n+1)\alpha). \end{aligned}$$

Substituting $\alpha = 3\pi/2$ into Eq. (17) yields a simplified form of the transcendental equation:

$$n^2 (1 - 4\kappa_0^2) + \sin^2 \left(\frac{3\pi n}{2} \right) (4n^2 \kappa_0^2 - 1) + \sin(3\pi n) (-2n\kappa_0) = 0, \quad (18)$$

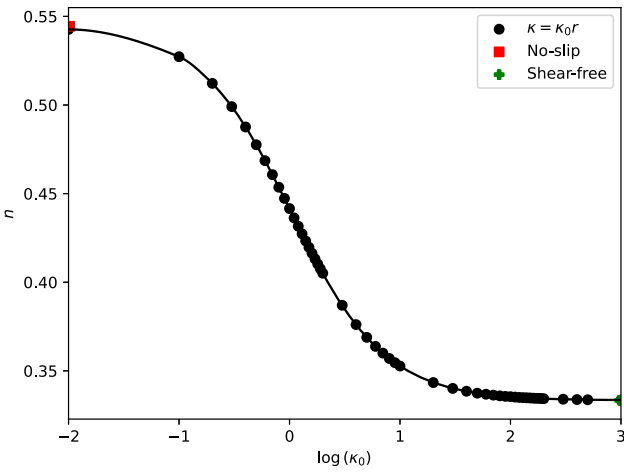


Fig. 2 Variation of n against κ_0

Table 1 Values of n for different slip coefficient κ_0

Slip constant κ_0	Eigenvalues n
0	0.5444
0.01	0.5426
0.1	0.5272
0.45	0.4825
1	0.4415
4.5	0.3723
10	0.3527
45	0.3380
100	0.3354
1000	0.3335

where the coefficients are now expressed as

$$\begin{aligned}
 A &= -C = -\frac{1}{2n}, \\
 C &= \frac{1}{2n}, \\
 D &= \frac{4n\kappa_0 + 2(n+1)\tan(\frac{3\pi n}{2})}{4n^2}, \\
 B &= \frac{\kappa_0[-A(n+1)^2 - C(n-1)^2] - D(n-1)}{n+1}.
 \end{aligned} \tag{19}$$

Figure 2 shows the smallest admissible eigenvalues as the parameter κ_0 varies. We note the versatility of this similarity solution as it interpolates between the no-slip case when $\kappa_0 = 0$ and the free-surface case as $\kappa_0 \rightarrow \infty$ (where we note that the C_0 in the stream function expression Eq. (8), needs to be scaled inversely with κ_0 in order to balance the growth of the eigenfunction and give a finite expression in this limit). The Table 1 shows that we are effectively in the free-surface case (at least to 4 d.p. in the eigenvalue) when $\kappa_0 = 10^3$.

To illustrate the behaviour of $f(\theta)$ in the streamfunction (8) as the value of κ_0 changes, we present in Fig. 3 the profile of f for some values of κ_0 . As expected, the values of $f(\theta)$ increase with κ_0 , since the constants B and D include terms that are proportional to κ_0 .

3.1.3 A comment on the theoretical validity of the similarity solutions

The streamfunction (8) has the order of magnitude estimate $\psi = \mathcal{O}(C_0 r^{n+1})$, assuming that $f(\theta)$ is of order unity. The orders of magnitude of the steady inertial acceleration $Re(\mathbf{v} \cdot \nabla) \mathbf{v} = \mathcal{O}(Re C_0^2 r^{2n-1})$ and the viscous force $\nabla^2 \mathbf{v} = \mathcal{O}(C_0 r^{n-2})$, suggest that the inertial term is negligible provided

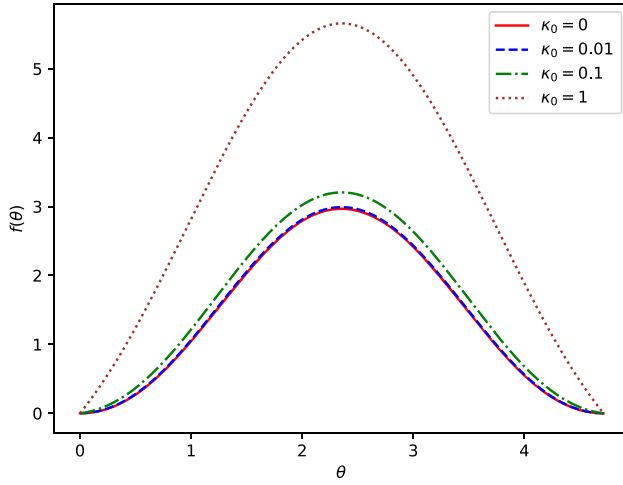


Fig. 3 Profile of $f(\theta)$ for some values of κ_0

$$Re C_0 r^{n+1} \ll 1. \quad (20)$$

Since $n > 0$ and C_0 is order one (or smaller), we would expect the approximation (8) to be valid for radial distances smaller than $Re^{-\frac{1}{n+1}}$. For small Reynolds numbers, this does not impose a significant length scale restriction, however as the Reynolds number increases, the applicable radial distance reduces. We note that, even for Reynolds numbers of order unity, the similarity solutions will still be valid for small enough radial distances.

The no-slip and varying slip coefficient boundary conditions do not impose a length scale restriction on the similarity solutions satisfying (20). However, in the constant slip case we only obtain a similarity solution for small radial distances, technically in the limit $r \rightarrow 0$. As in [33], we now formally need to pose an asymptotic expansion instead of (8) in positive powers of r , the leading order behaviour being self-similar and satisfying the shear-free boundary condition.

The presence of constant slip thus technically destroys the similarity solution of no-slip. The only way a similarity solution of similar form and valid for analogous radial distances is to introduce a specific radially dependent slip coefficient. It is worth drawing analogy with the Blasius similarity solution for solving Prandtl's boundary layer flow over a flat plate [29]. When slip is introduced on the plate [25], this classic similarity solution is lost, but can still be used in an approximate local sense by allowing key problem parameters (Knudsen and Reynolds numbers) to vary with distance along the plate in the slip plate condition. We note that this is not what we are doing here, where we are removing the distance dependence through use of an appropriate slip behaviour, which recaptures a self-similar solution behaviour. As a final remark, we note that the introduction of additional physical effects such as non-isothermal flow in the flat plate boundary layer problem, removes any trace of the classic similarity solution e.g. [8]. However, this may not be the fate of our corner flow self-similar solutions in applications such as viscoelastic flows, particularly for viscoelastic models in which the corner velocity flow is known to be Newtonian dominated e.g. Phan-Thien–Tanner [10,31] and Giesekus [9].

3.2 Numerical verification of the asymptotic results in the L-shaped flow

The streamfunction behaviour (8) gives a vanishing velocity field at the reentrant corner, but singular stresses since $0 < n < 1$. To validate this singular solution with $\mathbf{v} = \mathcal{O}(r^n)$, $\nabla \mathbf{v} = \mathcal{O}(r^{n-1})$ and $p = \mathcal{O}(r^{n-1})$, where n depends on κ_0 as detailed in Table 1, we conducted simulations of the L-shaped flow. This configuration, shown in Fig. 4, consists of two perpendicular channels: one horizontal and one vertical, each with a width of $1L$ and a length of $11L$. For the boundary conditions along the solid walls (see Fig. 4), the Navier slip condition (Eq. (4)) was applied, incorporating both the traditional slip coefficient κ and the proposed modification introducing the new slip constant κ_0 (Eq. (15)). In the numerical code, the modification proposed in Eq. (15) is applied exclusively to the walls near the singularity, restricted to the region where $r \leq 1$. Outside of this

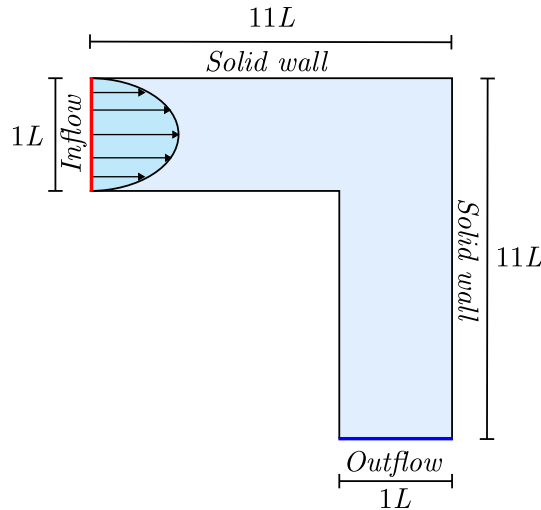


Fig. 4 L-shaped geometry. L is the characteristic length

region, the traditional constant κ is used. At the inflow boundary, the velocity profile follows the parabolic distribution characteristic of the Poiseuille flow. In the outflow, homogeneous Neumann boundary conditions were imposed on the velocity field. This geometry was chosen for its simplicity and the absence of corner vortices, which are typically present in benchmark flows such as the 4:1 planar contraction.

The simulations were performed at $Re = 0.01$ using four different values of κ_0 : 0, 0.45, 4.5, and 45. These values were selected to match the parameters employed in [15]. The numerical implementation relies on a finite difference method to discretize the Navier-Stokes equations (Eq. (6)) and employs a projection strategy to decouple velocity and pressure. More details on the numerical methodology can be found in our previous work [11, 12]. The computational mesh is non-uniform and refined in the vicinity of the corner, with the smallest cell measuring $\Delta_{x_{min}} = \Delta_{y_{min}} = 0.001$.

Figure 5 presents the numerical profiles of the velocity components u and v (first and second rows, respectively) and the pressure p (third row) along the radial distance r from the corner of the L-shaped geometry. The profiles were extracted at an angle of $\theta = \frac{3\pi}{4}$, which bisects the corner into two symmetric regions. The results in the first column correspond to simulations using the Navier slip law with constant slip $\kappa = \kappa_0$, while those in the second column use the modified slip coefficient $\kappa = \kappa_0 r$. For the constant case κ , the profiles adhere to the shear-free singularity condition, with the slopes remaining invariant, $n = \frac{1}{3}$, across different values of κ [32]. In contrast, the varying slip coefficient leads to variations in the slopes of u , v , and p as κ_0 changes, aligning with the predictions in Table 1.

As shown in Fig. 5, the velocity components u and v successfully capture the predicted asymptotic behaviour for both cases: constant slip coefficient and varying slip coefficient $\kappa = \kappa_0 r$. However, the pressure results deviate from the expected asymptotic behaviour in both scenarios, indicating the need for a finer mesh to accurately resolve the correct profiles. A similar issue with pressure was observed in Evans et al. [12], in their study of viscoelastic flow in a 4:1 planar contraction geometry under no-slip. However, we do note that the pressure behaviour improves dramatically as the slip constant increases.

4 Numerical simulations: 4:1 planar contraction and 1:4 planar expansion flows

To further understand the influence of the Navier slip boundary condition around the singularity, we propose two additional variations of the slip coefficient, complementing the cases of constant κ and $\kappa = \kappa_0 r$. The four slip boundary conditions considered in this study may be summarized as follows:

- Constant κ :

$$\kappa = \kappa_0. \quad (21)$$

This case represents the traditional Navier slip law, as used, for example, in Ferrás et al. [15].

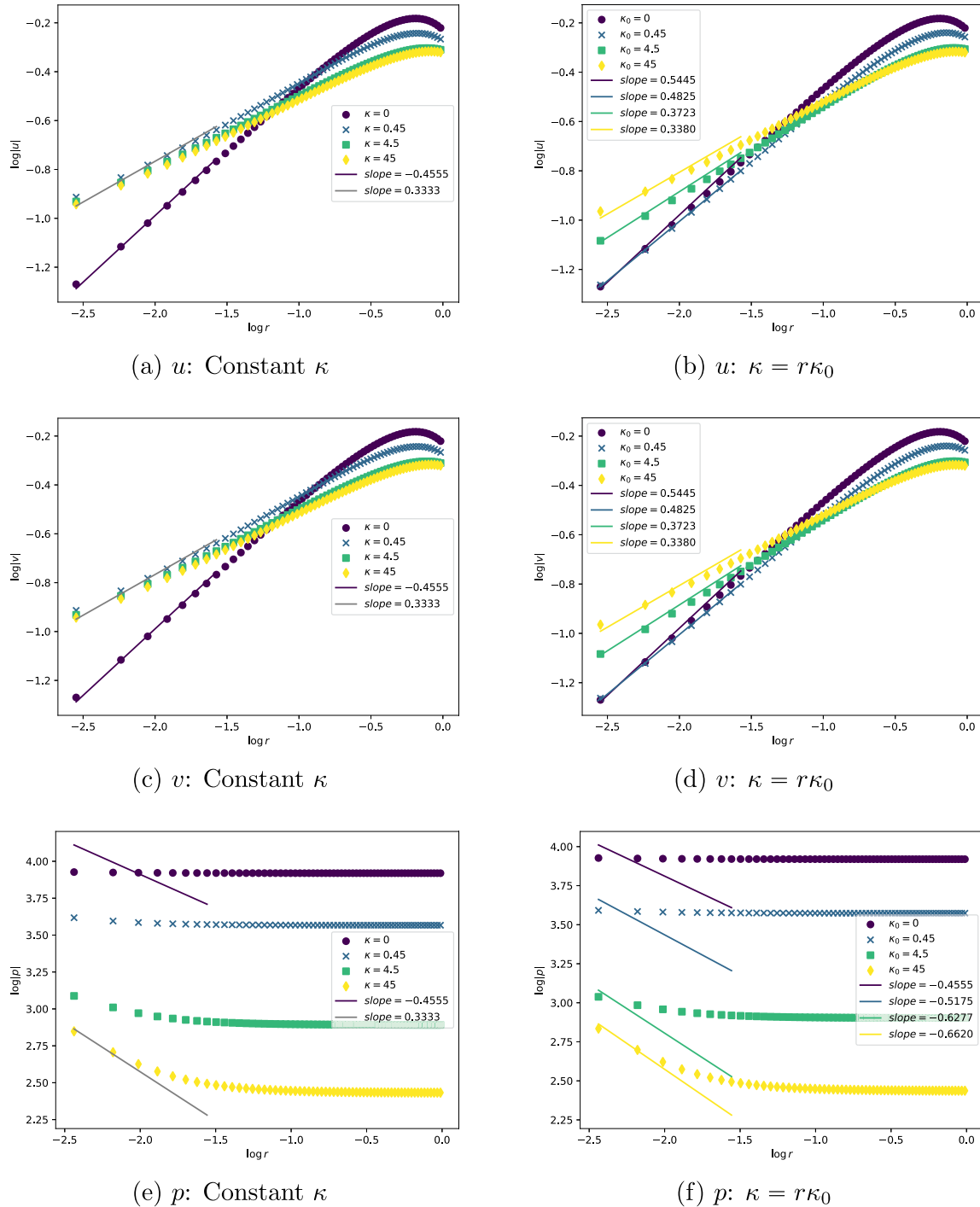


Fig. 5 L-shaped slopes at $\theta = 0.75\pi - \kappa$ (left), $\kappa = \kappa_0 r$ (right)

- κ as an increasing function of r :

$$\kappa = \begin{cases} r\kappa_0, & \text{if } 0 \leq r \leq 1, \\ \kappa_0, & \text{if } r > 1. \end{cases} \quad (22)$$

This slip condition modifies the coefficient κ to increase linearly with r within $r \leq 1$, as previously discussed in Section 3. It possesses the similarity behaviour of Section 3.1.2, and truncates the linear growth behaviour at $r = 1$. Consequently, distance varying slip only occurs local to the singularity with wall slip then being constant further away from the corner.

- κ as an increasing function of r with a fixed upper limit $\frac{\kappa_{\text{ext}}}{\kappa_0}$:

$$\kappa = \begin{cases} r\kappa_0, & \text{if } 0 \leq r \leq \frac{\kappa_{\text{ext}}}{\kappa_0}, \\ \kappa_{\text{ext}}, & \text{if } r > \frac{\kappa_{\text{ext}}}{\kappa_0}. \end{cases} \quad (23)$$

This behaviour extends Eq. (22) case by introducing an external limit $\frac{\kappa_{\text{ext}}}{\kappa_0}$, beyond which κ remains constant and equal to κ_{ext} . This introduces a new parameter κ_{ext} , external κ , that now allows for wall slip away from the singularity to be prescribed differently from the constant κ_0 . Since κ_0 controls the corner stress singularity, this form allows for independent setting of the wall slip away from the corner and the stress singularity. For this study, we take moderate slip $\kappa_{\text{ext}} = 10$ along the walls and examine the influence of changing the slip constant κ_0 .

- κ as a decreasing function of r :

$$\kappa = \begin{cases} (1 - r)\kappa_0, & \text{if } 0 \leq r \leq 1, \\ 0, & \text{if } r > 1. \end{cases} \quad (24)$$

This slip condition represents a reverse effect compared to the second and third cases, where slip is introduced locally to the singularity and transitioning to a no-slip condition as r increases beyond 1. Specifically, (24) gives $\kappa \sim \kappa_0$ as $r \rightarrow 0$, so that locally to the corner we have the shear-free condition of Section 3.1.1. This type of behaviour is introduced for a moving contact line singularity, where it is argued that slip is introduced locally to alleviate an unphysical stress singularity [4, 16, 17, 22]. Although we are dealing with a static singularity and do not have a free surface, we investigate this idea here to provide contrast to the previous cases in order to build a better understanding of the effect of the corner singularity on the flow.

Figure 6 illustrates the variation of κ with r for these four boundary conditions. For this illustration, κ_0 is initially fixed at 1. The black color with cross symbols represents the constant κ case, Eq. (21), where $\kappa = 1$ remains constant along the entire solid wall. The second condition, represented by red circles, Eq. (22), exhibits a linearly increasing behaviour around the singularity for $0 \leq r \leq 1$, and then, for $r > 1$, it stabilizes at a constant value $\kappa_0 = 1$. The third slip case, represented by green stars, Eq. (23), follows a similar approach to the previous condition, except that the region where the linear slip coefficient $\kappa = r\kappa_0$ is applied varies according to the ratio $\kappa_{\text{ext}}/\kappa_0$. The fixed value away from the singularity, for $r > \kappa_{\text{ext}}/\kappa_0$, is set here as $\kappa_{\text{ext}} = 2$ (purely for illustration, instead of 10, which is used in the numerical simulations below). Additionally, to further illustrate the behaviour in the region where κ_{ext} is applied, we consider two additional values for κ_0 : 1.25 and 0.75. This demonstrates that the location, given by $r = \kappa_{\text{ext}}/\kappa_0$, increases as κ_0 decreases. Finally, the so-called reverse condition, Eq. (24), represented in the graph by blue triangles, exhibits a linearly decreasing behaviour for $0 \leq r \leq 1$, and then, away from the singularity for $r > 1$, the value is fixed at $\kappa = 0$, which corresponds to the no-slip boundary condition.

For the functions considered, it is convenient to refer to the radial location at which the function changes behaviour (i.e. possesses a discontinuous slope) as the transition point in behaviour. Thus for (22) and (24) it is at $r = 1$, whilst for (23) it is $r = \kappa_{\text{ext}}/\kappa_0$.

To analyze the effects of the four different slip boundary conditions, we perform simulations on two benchmark problems: the 4:1 planar contraction and the 1:4 planar expansion. In these geometries, the wider channel has a width of $8L$, while the narrower channel measures $2L$ in width. Each channel is $40L$ long. These geometries, representing half of the domain, are illustrated in Figure 7. The inflow condition for the velocity field is consistent with that used in the L-shaped flow presented in Subsection 3.2, featuring a parabolic profile. The maximum velocity at the inflow is set to 0.375 for the 4:1 contraction and 1.5 for the 1:4 expansion. At the outflow boundary, a homogeneous Neumann condition is applied to the velocity field. On the solid surfaces, all four slip boundary conditions are implemented and compared. For both geometries, the simulations are

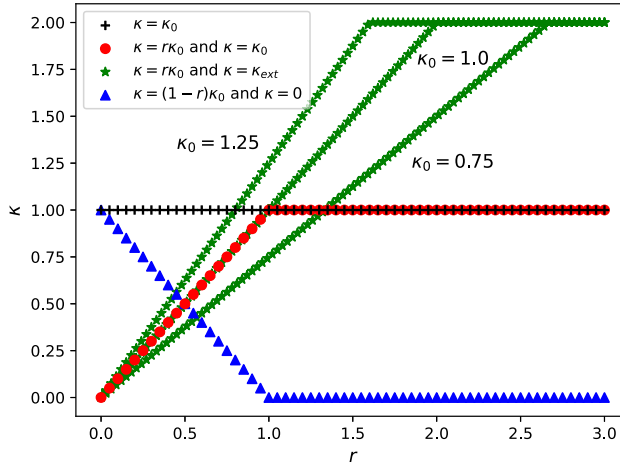


Fig. 6 Variation of κ with r for the four different slip boundary conditions (Eqs. (21)–(24)). Parameters used: $\kappa_0 = 1$, $\kappa_{\text{ext}} = 2$

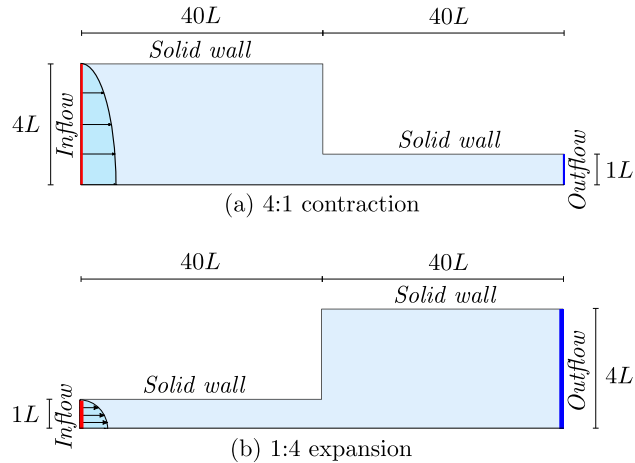


Fig. 7 Schematic of the (a) 4:1 contraction and (b) 1:4 expansion geometry. L represents the characteristic length scale

carried out on a non-uniform grid, which is maximally refined at the corners, featuring a minimum spacing of $\Delta x_{\min} = \Delta y_{\min} = 0.0001$.

4.1 Vortex size

Figure 8 illustrates the variation in vortex size, X_R , for both the 4:1 contraction (Figure 8(a)) and the 1:4 expansion (Figure 8(b)), as a function of the logarithm of different values of the slip coefficient κ_0 . It can be observed that, for all slip boundary conditions, the vortex size becomes smaller as the slip coefficient grows, except for the reverse slip condition (Eq. (24)), which remains approximately constant with changes in κ_0 . This behaviour aligns with the results obtained using a no-slip boundary condition. The findings from Ferrás et al. [14,15] are also included in Figure 8 for comparison, showing consistency with the results for the constant κ (Eq. (21)) and $\kappa = \kappa_0 r$ (Eq. (22)) cases. We note that the external κ case (23) behaviour is relatively constant once κ_0 exceeds unity, indicating the relative insensitivity of the vortex size to the change in stress singularity. For smaller values of κ_0 the transition point of the function is sufficiently far from the singularity to encroach upon the corner vortex and influence its size.

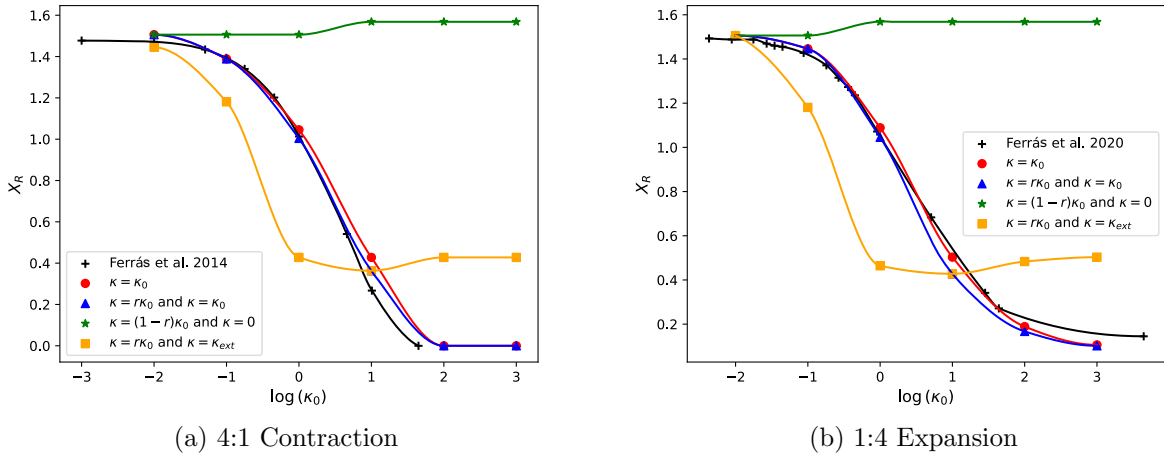


Fig. 8 Variation of the vortex size X_R with $\log(\kappa_0)$ (the lines are just a guide to the eye)

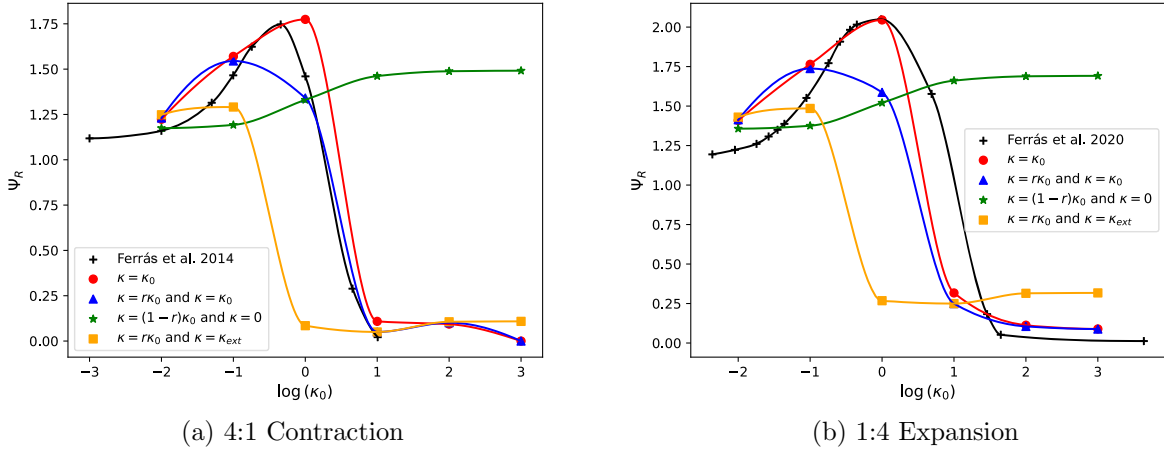


Fig. 9 Variation of the vortex intensity Ψ_R with $\log(\kappa_0)$ (the lines are just a guide to the eye)

4.2 Vortex intensity

The vortex intensity Ψ_R , representing the strength of a vortex, is defined based on the streamfunction at the vortex center ψ_R and normalized by UL , the inlet flux per unit depth:

$$\Psi_R = \frac{\psi_R - UL}{UL} \times 10^3, \quad (25)$$

where ψ_R is the streamfunction value at the vortex center. Fig. 9 illustrates the variation of Ψ_R with the logarithm of κ_0 . Except for the reverse slip condition, Eq. (24), all other slip cases exhibit a rise in vortex intensity for small values of κ_0 , reaching a peak before declining to zero. The value of κ_0 at which the peak occurs varies between conditions. In contrast, the reverse slip condition exhibits a slow and continuous increase with κ_0 . The results of Ferrás et al. [14, 15] are included in the figures for comparison. Unlike previous cases, results of Ferrás et al. [14, 15] show a quantitative deviation from the constant κ scenario, which we attribute to differences in numerical methodologies. As for the vortex size, the response to the external (23) slip behaviour is relatively constant once κ_0 exceeds unity, indicating again the relative insensitivity of intensity to the change in stress singularity.

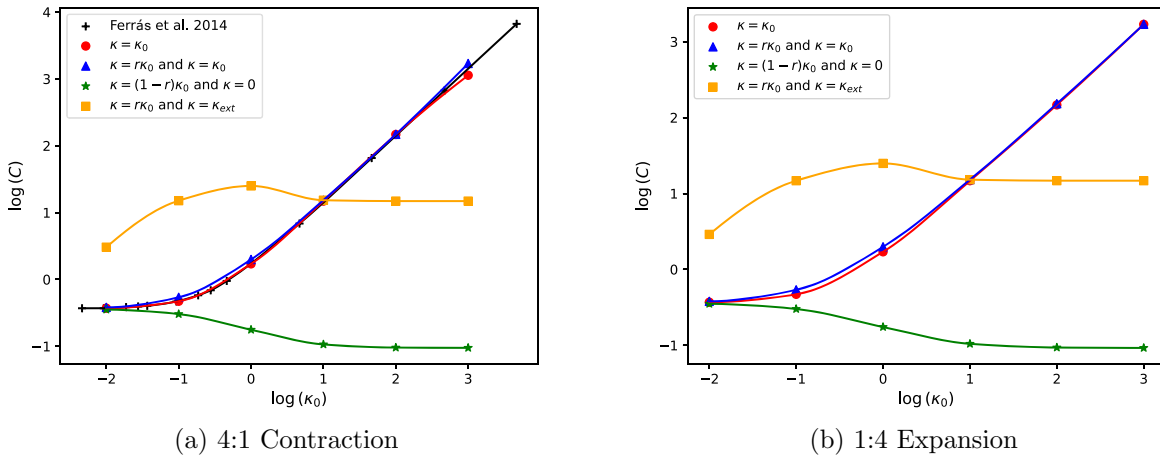


Fig. 10 Variation of Couette correction $\log C$ with $\log (\kappa_0)$ (the lines are just a guide to the eye)

4.3 Couette correction

The Couette correction, or excess pressure drop [5], is defined as:

$$C = \frac{\Delta P - \Delta P_1 - \Delta P_2}{2\tau_w}, \quad (26)$$

where ΔP is the total pressure drop, ΔP_1 and ΔP_2 are the pressure drops for fully developed flow in the upstream and downstream channels, respectively, and τ_w is the wall shear stress. Figure 10 shows the behaviour of the Couette correction with respect to the logarithm of the slip coefficient κ_0 . The behaviour for the constant κ , Eq. (21), and $\kappa = r\kappa_0$, Eq. (22), shows similar trends and aligns with the results presented by Ferrás et al. [14] for the 4:1 contraction flow, with C increasing as κ_0 increases. For the reverse κ case, some variation is observed for small κ_0 , but for $\kappa_0 > 10$, the results become relatively constant. The external κ case follows a similar trend to that observed for the vortex size and intensity, with relative insensitivity of the Couette correction to κ_0 , once the transition point is sufficiently close to the reentrant corner i.e. $\kappa_0 > 1$.

4.4 Drag and Loss coefficients

The drag coefficient K_D for the contraction flow (or loss coefficient K_L for the expansion flow) is defined as the ratio between the drag force and the kinetic energy, and is expressed as:

$$K_D = \frac{F_D}{\frac{1}{2}\rho U_{\text{ref}}^2 A_{\text{ref}}}, \quad (27)$$

where F_D is the drag force, calculated as the sum of the pressure and shear stress integrals along the wall located at $x = 40L$. However, for the vertical wall of the contraction, the shear stress acts in the transverse (y) direction, tangential to the wall, and not in the streamwise (x) direction. As a result, the shear stress does not contribute to the drag in the flow direction, and the drag force is determined solely by the pressure distribution. The terms U_{ref} and A_{ref} represent the reference velocity and reference area, respectively. The reference velocity is obtained by integrating the velocity profile over the inflow section, while the reference area is defined as the product of the height difference between the upstream and downstream channels of the contraction and a unit depth ($1L$). For the contraction flow, the reference velocity is $U_{\text{ref}} = 0.25U$, whereas for the expansion flow it is $U_{\text{ref}} = 1U$. The reference area is the same for both flow configurations, with $A_{\text{ref}} = 6L^2$, since the magnitude of the difference between the upstream and downstream channel heights is identical in both cases.

Table 2 presents the values of the drag coefficient K_D for the four slip condition strategies, Eqs. (21)–(24), and for a range of slip coefficients $\kappa_0 = 0, 0.01, 0.1, 1, 10, 100, 1000$. As shown in Table 2, the drag coefficient decreases with increasing values of κ_0 . This trend is expected, as the only term that varies in Eq. (27) is the drag force, which depends on the pressure distribution. As the slip coefficient increases, the pressure along the vertical wall decreases, resulting in a lower drag force.

Table 2 Drag coefficient K_D for the 4:1 contraction in scientific notation

κ, κ_0	$\kappa = \kappa_0$	$\kappa = r\kappa_0$	$\kappa = r\kappa_0$ and $\kappa = \kappa_{ext}$	$\kappa = (1 - r)\kappa_0$ and $\kappa = 0$
0	3.938×10^5	3.938×10^5	3.938×10^5	3.938×10^5
0.01	3.828×10^5	3.830×10^5	2.635×10^5	3.937×10^5
0.1	3.067×10^5	3.074×10^5	3.145×10^4	3.929×10^5
1	1.090×10^5	1.100×10^5	3.146×10^4	3.907×10^5
10	2.537×10^4	2.558×10^4	2.558×10^4	3.895×10^5
100	1.423×10^4	1.425×10^4	2.537×10^4	3.893×10^5
1000	1.308×10^4	1.308×10^4	2.537×10^4	3.893×10^5

Table 3 Loss coefficient K_L for the 1:4 expansion according to the slip boundary condition

κ, κ_0	$\kappa = \kappa_0$	$\kappa = r\kappa_0$	$\kappa = r\kappa_0$ and $\kappa = \kappa_{ext}$	$\kappa = (1 - r)\kappa_0$ and $\kappa = 0$
0	2.079×10^2	2.079×10^2	2.079×10^2	2.079×10^2
0.01	2.002×10^2	2.048×10^2	1.605×10^2	2.026×10^2
0.1	1.629×10^2	1.802×10^2	3.488×10^0	1.890×10^2
1	1.451×10^1	3.748×10^1	-1.182×10^2	1.696×10^2
10	-1.514×10^2	-1.458×10^2	-1.457×10^2	1.619×10^2
100	-1.890×10^2	-1.883×10^2	-1.511×10^2	1.608×10^2
1000	-1.933×10^2	-1.932×10^2	-1.514×10^2	1.607×10^2

As highlighted in the previous analysis, the results for the constant slip condition (Eq. (21)) and the modified slip condition (Eq. (22)) are very similar across all values of κ_0 . In contrast, the external slip case (Eq. (23)) reaches an almost constant drag coefficient for $\kappa_0 > 1$, which is consistent with earlier observations. Finally, the decreasing slip case (Eq. (24)) exhibits behaviour similar to the no-slip case, showing only a slight reduction in drag coefficient as κ_0 increases.

Table 3 presents the loss coefficient K_L , defined analogously to the drag coefficient K_D in Eq. (27), but applied to the expansion flow. The values of K_L differ significantly from those of K_D , as expected, given their distinct physical interpretations and the use of different reference velocities U_{ref} in their calculation. Nevertheless, the variation of K_L across the different slip condition strategies exhibits a similar qualitative behaviour to that observed for K_D .

It is worth noting that, to the best of our knowledge, the drag coefficient in the specific context of planar contraction flow, i.e., flow entering a two-dimensional contraction channel, has not been reported in the literature. Therefore, the drag and loss coefficient results presented in this work may serve as a valuable reference for code verification and future investigations.

4.5 Verification of the asymptotic behaviour

The asymptotic results derived in Section 3 are now verified through simulations of Newtonian flow in contraction and expansion geometries. Similar to the verifications done in Subsection 3.2, the slopes of the u and v velocity components, along with pressure p , are plotted along the line $\theta = \frac{\pi}{2}$ at the bottom singularity, considering $0 \leq r \leq 1$.

Fig. 11 presents the numerical verification for the four slip boundary conditions in a planar 4:1 contraction flow. The results for the u velocity component accurately capture the expected asymptotic slopes for all boundary conditions, while the v velocity component shows deviations for values of κ_0 greater than 1. In contrast, the pressure results (third column) improve as κ_0 increases beyond 1.

It can be noted from Fig. 11 that the constant κ and reverse slip conditions exhibit zero-shear stress behaviour around the singularity, whereas the $\kappa = \kappa_0 r$ and external κ_{ext} conditions follow the slopes derived in Section 3. It is also worth mentioning that the pressure results for the reverse slip condition deviate significantly from the expected asymptotic behaviour. A similar observation was made in [12] for PTT and Giesekus viscoelastic flows in a 4:1 planar contraction. This indicates a need for an improved treatment of the pressure variable in the numerical scheme when imposing no-slip.

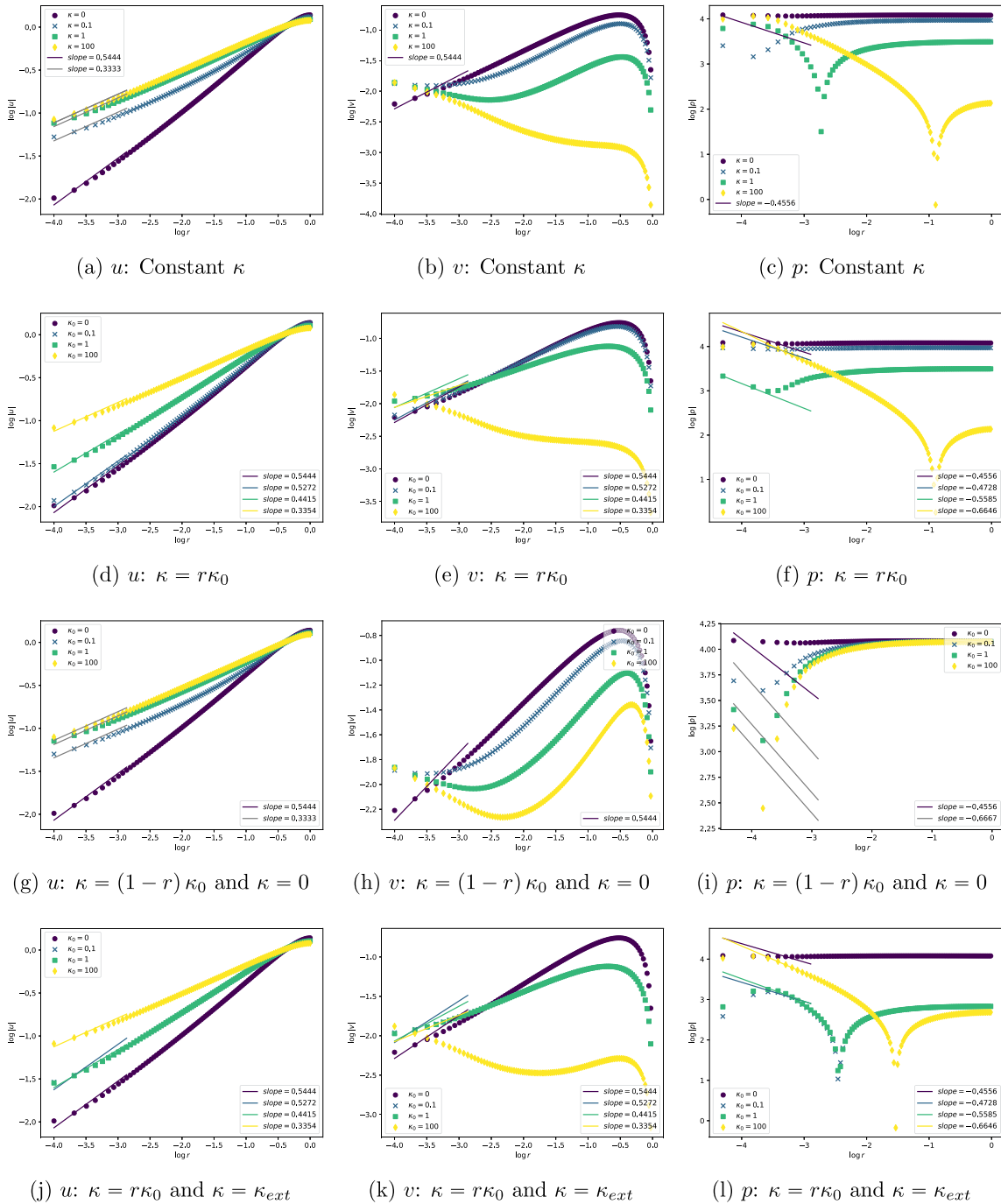


Fig. 11 Numerical verification of the asymptotic behaviour for velocity components u (first column), v (second column) and p (third column) in a 4:1 planar contraction flow

The results for the 1:4 planar expansion follow the same behaviour as the 4:1 planar contraction, as shown in Fig. 12, with the exception of the pressure results, which follow the expected asymptotic behaviour for all slip boundary cases. Additionally, it is worth noting that the pressure results improve as the value of κ_0 increases.

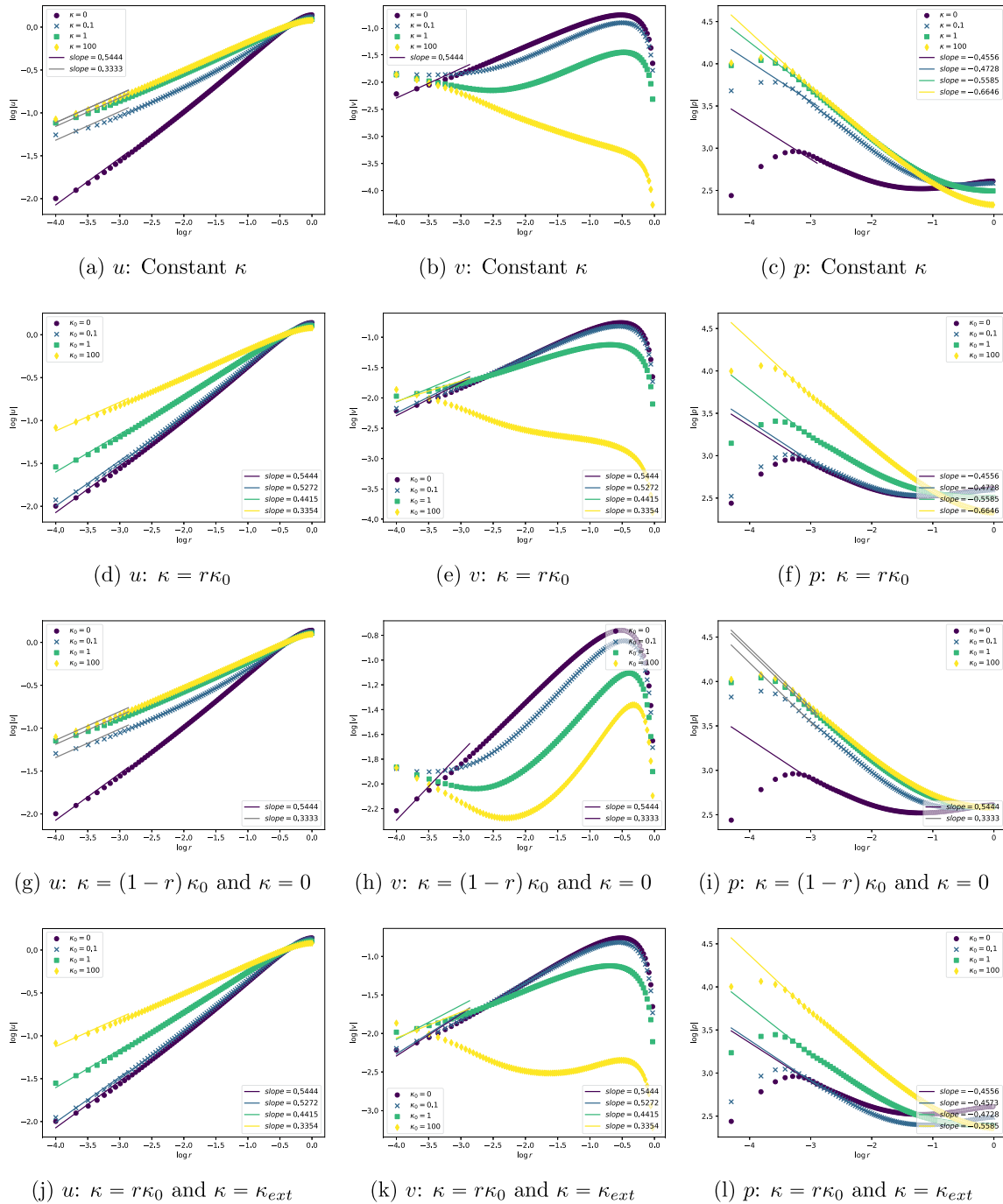


Fig. 12 Numerical verification of the asymptotic behaviour for velocity components u (first column), v (second column) and p (third column) in a 1:4 planar expansion flow

4.6 Flow type

Both Figures 13 and 14 present colormaps representing the value of flow type ξ , Eq. (28), for contraction and expansion flows, respectively. Analysis of these figures allows for the identification of regions dominated by each flow type, providing insights into the fluid behaviour in these geometries. In order to quantify the nature of the flow in different regions, a commonly used flow-type parameter [24] is

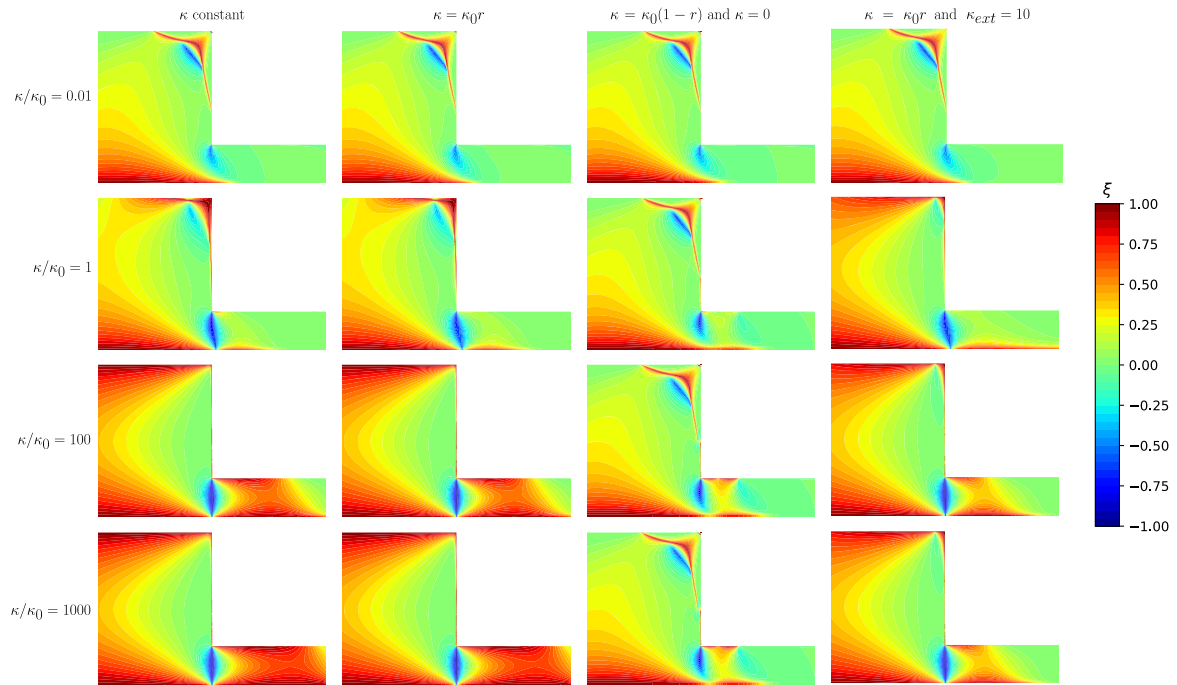


Fig. 13 Flow-type parameter for the 4:1 planar contraction flow

$$\xi = \frac{|\mathbf{D}| - |\mathbf{W}|}{|\mathbf{D}| + |\mathbf{W}|}, \quad (28)$$

where $|\mathbf{D}|$ is the magnitude of the rate of strain tensor ($|\mathbf{D}| = \sqrt{1/2\text{tr}\mathbf{D}^2}$, or equivalently, the Frobenius norm of \mathbf{D}) and $|\mathbf{W}|$ is the magnitude of the vorticity tensor, $\mathbf{W} = \frac{1}{2}(\nabla\mathbf{v} - \nabla\mathbf{v}^\top)$, given by $|\mathbf{W}| = \sqrt{1/2(\mathbf{W} : \mathbf{W}^\top)}$. The flow-type parameter ranges from -1 , corresponding to solid-body rotation, to 1 , representing pure extensional flow, passing through 0 , which indicates simple shear flow.

Figure 13 explicitly illustrates how varying the value of κ/κ_0 influences the flow type in the contraction, according to different slip boundary conditions. We note a very similar behaviour in columns 1, 2 and 4, where increasing the slip coefficient leads to the dominance of extensional flow, especially near the top wall and at the center of the reentrant channel. It is also noteworthy that the boundary condition in column 4 exhibits extensional flow dominance as early as κ/κ_0 transitions from 0.1 to 1 , while in columns 1 and 2, this behaviour only emerges at $\kappa/\kappa_0 = 100$. This dominance is less present in column 4 for values of $\kappa/\kappa_0 = 100$ and 1000 , where simple shear is still present. On the other hand, the colormaps in column 3 show that extensional flow predominantly increases near the reentrant corner, especially along the right side and the top channel walls. Solid-body rotation, present near the corner singularity, is observed to extend towards the center of the channel, but, unlike in previous cases, it does not fully reach the channel center.

The results for the expansion, presented in Figure 14, are broadly similar to those observed for the contraction case. A key difference, however, lies in column 4, where extensional flow dominance only becomes apparent when κ/κ_0 reaches a value of 1 or higher. This indicates that a greater degree of slip is necessary to establish extensional flow dominance in this specific boundary condition.

5 Conclusions

In this study, we considered a slip coefficient-dependent similarity solution for a Newtonian flow around a sharp corner. This solution extends the similarity solution for the standard Navier slip condition, Eq. (21), in which the slip boundaries behave like free-surfaces. This allowed us to modify the singular behaviour by adjusting the slip coefficient κ_0 and to interpolate continuously between the two extreme cases of no-slip and a free-surface. As a result, we could investigate the influence of the reentrant corner singularity on aspects of the flow. The main conclusions may be summarised as follows:

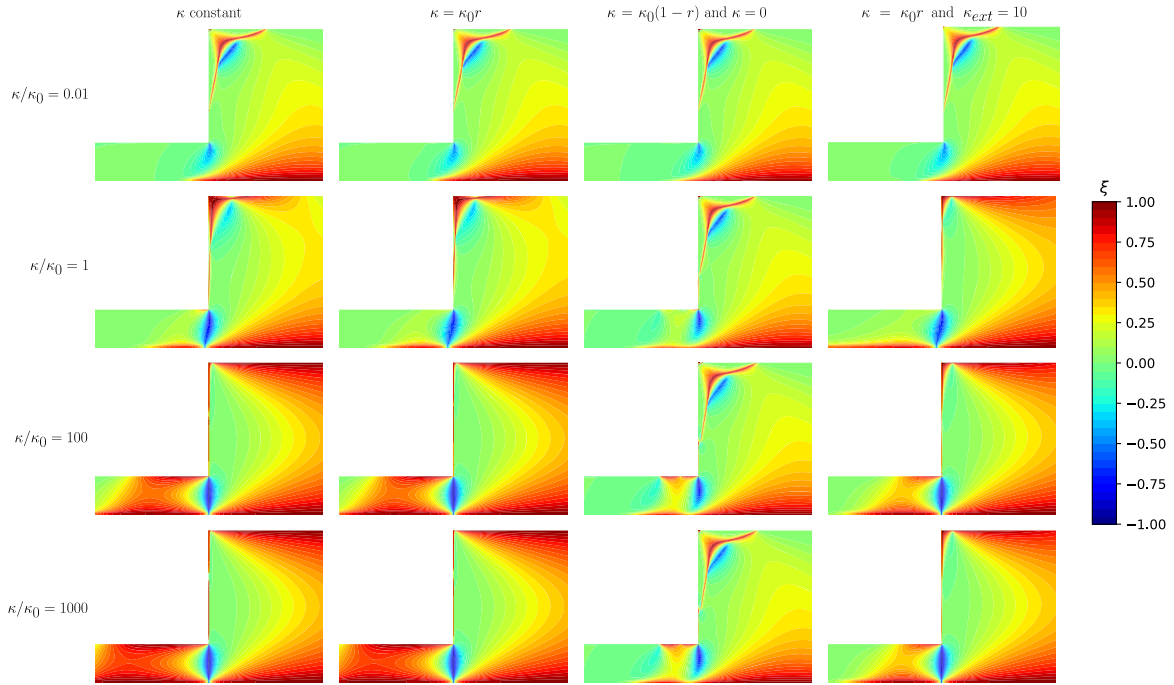


Fig. 14 Flow-type parameter for the 1:4 planar expansion flow

1. Changing boundary conditions from no-slip to slip significantly impacts the overall flow behaviour. This is clearly demonstrated by the flow type parameter ξ in (28) in both the contraction Figure 13 and expansion Figure 14. It is also evident that modifying the constant slip condition (21) near the reentrant corner to (22) has no discernible effect.
2. Comparisons involving boundary conditions Eq. (21) and Eq. (22) reveal that the singularity behaviour does not substantially influence the flow properties when wall slip is imposed. For instance, the vortex size, vortex intensity, and Couette correction under conditions (21) and (22) are very similar. Further, the insensitivity of these quantities in the external κ case is apparent for $\kappa_0 > 1$ (once the transition point is sufficiently close to the reentrant corner). Thus changing the reentrant corner singularity strength when wall slip is imposed has little influence on global aspects of the flow.
3. However, this is not true when we introduce local slip at the singularity in otherwise no-slip flows. The quantities of vortex size, intensity and Couette correction all change as the slip parameter κ_0 varies in the reverse slip case (24).

It remains to be seen whether similar conclusions apply to non-Newtonian flows. As future work, we plan to investigate the effects of various Navier slip laws in conjunction with viscoelastic models.

Acknowledgements J.D. Evans acknowledges financial support from FAPESP-SPRINT grants 2018/22242-0 and 2024/01651-0, and would like to thank the University of Bath for sabbatical leave during 2023-2024. I.L. Palhares Junior and C.M. Oishi would like to acknowledge support from CEPID-CeMEAI (FAPESP Grant No. 2013/07375-0), FAPESP-SPRINT Grant No. 2024/01651-0, FAPESP-ANR Grant No. 2024/04769-1, and the National Council for Scientific and Technological Development (CNPq), grants #307228/2023-1. F. Ruano Neto acknowledges the financial support of FAPESP Grant No. 2021/05727-2. The authors also acknowledge the Numerical Simulation and AI Laboratory at FCT/UNESP for their support with cluster resources. Research carried out using the computational resources of the Center for Mathematical Sciences Applied to Industry (CeMEAI) funded by FAPESP (grant 2013/07375-0).

Declarations

Author Contribution J.E., I.P, C.O. and F.R.N wrote the main manuscript text and I.P and F.R. prepared all figures. All authors reviewed the manuscript.

Data Availability No datasets were generated or analysed during the current study.

Competing interests The authors declare no competing interests.

Appendix A. Convergence test

A mesh convergence study was conducted for the L-shaped channel. For simplicity of notation, let $\Delta_{min} = \Delta_{x_{min}} = \Delta_{y_{min}}$ denote the minimum grid spacing. Three non-uniform meshes were considered, characterized by their minimum spacing: a coarse mesh $M1$ with $\Delta_{min} = 0.01$, a medium mesh $M2$ with $\Delta_{min} = 0.005$, and a reference mesh M_{ref} with $\Delta_{min} = 0.001$. The reference mesh is the same as that used in the simulations presented in Section 3.2. The slip boundary condition considered for this study is that of (22). Figure 15 shows the profile of the v -velocity component along the line $x \in [10, 11]$ at $y = 5$. The close agreement of the results for the finer meshes provides qualitative evidence of mesh convergence. This is confirmed quantitatively in Table 4, which presents the Root Mean Squared Error (RMSE) for each mesh, showing reduction in error as the grid is refined.

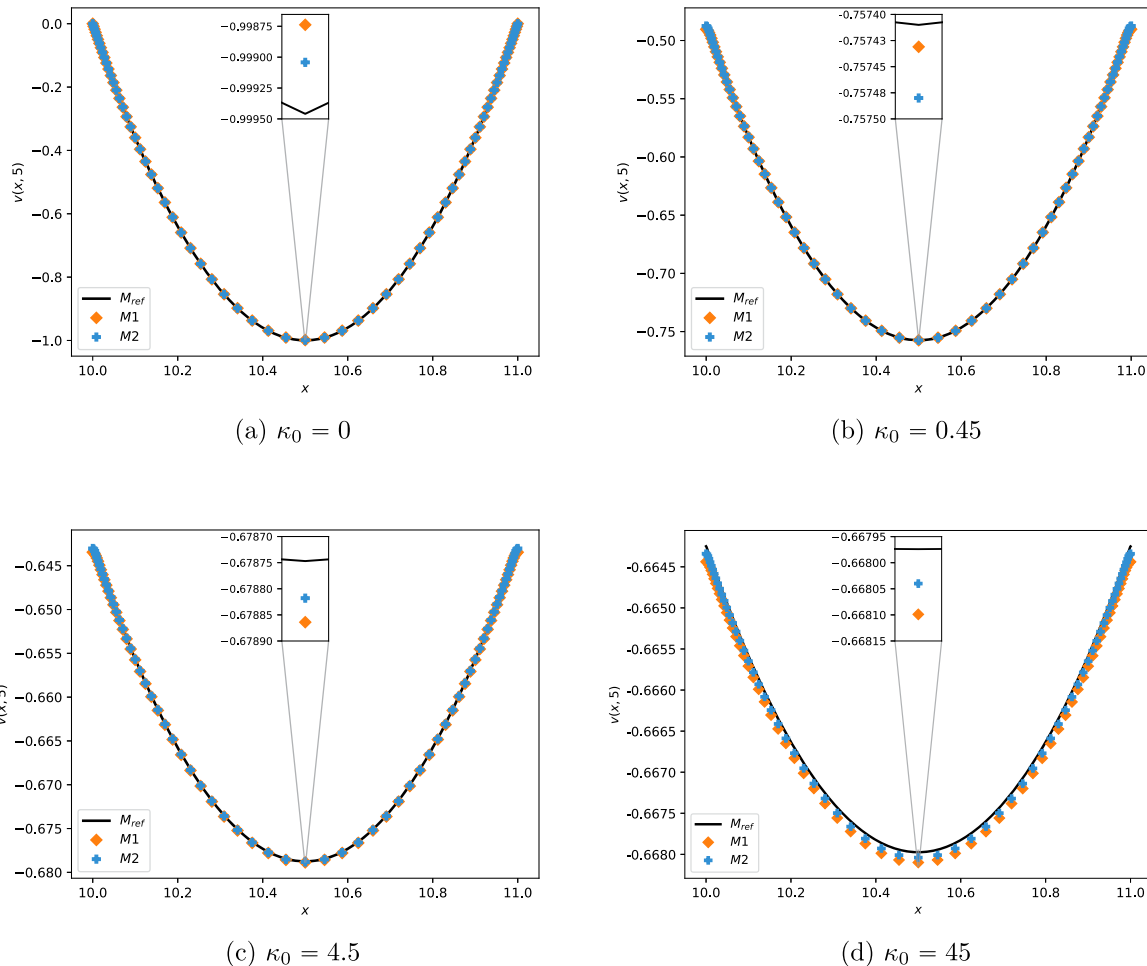


Fig. 15 Velocity profiles (v -component) for simulations using the slip boundary condition $\kappa = \kappa_0 r$

Table 4 Errors (RMSE) for the v -velocity taking M_{ref} as the reference

κ_0	$M1$	$M2$
0	3.389×10^{-4}	1.835×10^{-4}
0.45	9.776×10^{-4}	3.378×10^{-4}
4.5	1.893×10^{-4}	7.245×10^{-5}
45	1.281×10^{-4}	6.421×10^{-5}

References

- Azese, M.N.: On the detection, measurement, and characterization of slip-velocity in couette-rheology involving viscoelastic liquids. *Phys. Fluids* **31**, 023101 (2019)
- Barenblatt, G.I.: *Scaling, Self-similarity, and Intermediate Asymptotics*. Cambridge University Press (1996)
- Bhatti, K., Bano, Z., Siddiqui, A.M.: Analysis of slip effects on slow viscoelastic flow of second order fluid through a small diameter permeable tube. *Chin. J. Phys.* **77**, 632–645 (2022)
- Huh, C., Mason, S.G.: The steady movement of a liquid meniscus in a capillary tube. *J. Fluid Mech.* **81**(03), 401 (1977)
- Coates, P.J., Armstrong, R.C., Brown, R.A.: Calculation of steady-state viscoelastic flow through axisymmetric contractions with the eeme formulation. *J. Nonnewton. Fluid Mech.* **42**(1–2), 141–188 (1992)
- Dean, W.R., Montagnon, P.E.: On the steady motion of viscous liquid in a corner. *Math. Proc. Cambridge Philos. Soc.* **45**(3), 389–394 (1949)
- Drapaca, C.S.: Poiseuille flow of a non-local non-newtonian fluid with wall slip: a first step in modeling cerebral microaneurysms. *Fractal and Fractional* **2**(1), 9 (2018)
- Essaghir, E., Haddout, Y., Oubarra, A., Lahjomri, J.: Non-similar solution of the forced convection of laminar gaseous slip flow over a flat plate with viscous dissipation: linear stability analysis for local similar solution. *Meccanica* **51**(1), 99–115 (2016)
- Evans, J.D.: Re-entrant corner behaviour of the giesekus fluid with a solvent viscosity. *J. Nonnewton. Fluid Mech.* **165**(9–10), 538–543 (2010)
- Evans, J.D.: Re-entrant corner behaviour of the PTT fluid with a solvent viscosity. *J. Nonnewton. Fluid Mech.* **165**(9–10), 527–537 (2010)
- Evans, J.D., França, H.L., Palhares Junior, I.L., Oishi, C.M.: Testing viscoelastic numerical schemes using the oldroyd-b fluid in newtonian kinematics. *Appl. Math. Comput.* **387**, 125106 (2020)
- Evans, J.D., Palhares Junior, I.L., Oishi, C.M., Ruano Neto, F.: Numerical verification of sharp corner behavior for giesekus and phan-thien-tanner fluids. *Phys. Fluids* **34**(11), 113106 (2022)
- Ferrás, L., Afonso, A., Nóbrega, J., Pinho, F.: A numerical and theoretical study on viscoelastic fluid slip flows. *Phys. Fluids* **29**(5), 053102 (2017)
- Ferrás, L.L., et al.: Slip flows of newtonian and viscoelastic fluids in a 4:1 contraction. *J. Nonnewton. Fluid Mech.* **214**, 28–37 (2014)
- Ferrás, L.L., et al.: Newtonian and viscoelastic fluid flows through an abrupt 1:4 expansion with slip boundary conditions. *Phys. Fluids* **32**, 043103 (2020)
- Hocking, L.M.: A moving fluid interface on a rough surface. *J. Fluid Mech.* **76**(4), 801–817 (1976)
- Hocking, L.M.: A moving fluid interface. part 2. the removal of the force singularity by a slip flow. *J. Fluid Mech.* **79**(2), 209–229 (1977)
- Housiadas, K.D., Beris, A.N.: Viscoelastic flow with slip in a hyperbolic channel. *J. Rheol.* **68**(3), 415–428 (2024)
- Joshi, Y.M., Denn, M.M.: Planar contraction flow with a slip boundary condition. *J. Nonnewton. Fluid Mech.* **114**(2–3), 185–195 (2003)
- Karapetsas, G., Mitsoulis, E.: Some experiences with the slip boundary condition in viscous and viscoelastic flows. *J. Nonnewton. Fluid Mech.* **198**, 96–108 (2013)
- Khader, S., Mziou, M.M.: Chebyshev spectral method for studying the viscoelastic slip flow due to a permeable stretching surface embedded in a porous medium with viscous dissipation and non-uniform heat generation. *Boundary Value Problems*, **2017**, 37 (2017)
- Kulkarni, Y.: Stream function solutions for some contact line boundary conditions: navier slip, super slip and the generalized navier boundary condition. *Proc. Royal Soc. Math. Phys. Eng. Sci.* **479**(2278), 20230141 (2023)
- Lauga, M.P., Brenner, H.A., Stone, E.: Microfluidics: the no-slip boundary condition. Arxiv preprint [arXiv:cond-mat/0501557](https://arxiv.org/abs/0501557) (2005)
- Lee, J.S., Dylla-Spears, R., Teclemariam, N.P., Muller, S.J.: Microfluidic four-roll mill for all flow types. *Appl. Phys. Lett.* **90**(7), 074103 (2007)
- Martin, M.J., Boyd, I.D.: Blasius boundary layer solution with slip flow conditions. *AIP Conf. Proc.* **585**(1), 518–523 (2001)
- Moffatt, H.K.: Viscous and resistive eddies near a sharp corner. Technical Report 1 (1964)
- Navier, C.L.M.H.: Mémoire sur les lois du mouvement des fluides. *Mémoires de l'académie royale des sciences de l'institut de france* **6**, 389–440 (1822)
- Neto, C.: Boundary slip in newtonian liquids: a review of experimental studies. *Rep. Prog. Phys.* **68**(12), 2859–2897 (2005)
- Ockendon, H., Ockendon, J.R.: *Viscous Flow*. Cambridge Texts in Applied Mathematics. Cambridge University Press (1995)
- Pal, S., Samanta, A.: Role of slip in the stability of viscoelastic liquid flow through a channel. *Eur. J. Mechanics-B/Fluids* **101**, 118–130 (2023)
- Renardy, M.: Re-entrant corner behavior of the PTT fluid. *J. Nonnewton. Fluid Mech.* **69**(1), 99–104 (1997)

32. Salamon, T.R., Bornside, D.E., Armstrong, R.C., Brown, R.A.: The role of surface tension in the dominant balance in the die swell singularity. *Phys. Fluids* **7**(10), 2328–2344 (1995)
33. Salamon, T.R., Bornside, D.E., Armstrong, R.C., Brown, R.A.: Local similarity solutions for the stress field of an oldroyd-b fluid in the partial-slip/slip flow. *Phys. Fluids* **9**(8), 2191–2209 (1997)
34. Salamon, T.R., Bornside, D.E., Armstrong, R.C., Brown, R.A.: Local similarity solutions in the presence of a slip boundary condition. *Phys. Fluids* **9**(5), 1235–1247 (1997)

Publisher's Note Springer Nature remains neutral with regard to jurisdictional claims in published maps and institutional affiliations.

Springer Nature or its licensor (e.g. a society or other partner) holds exclusive rights to this article under a publishing agreement with the author(s) or other rightsholder(s); author self-archiving of the accepted manuscript version of this article is solely governed by the terms of such publishing agreement and applicable law.